Composites Science and Technology 200 (2020) 108460

Contents lists available at ScienceDirect

Composites Science and Technology

journal homepage: http://www.elsevier.com/locate/compscitech

An enriched cohesive law using plane-part of interfacial strains to model intra/inter laminar coupling in laminated composites

Ping Hu, Ditho Pulungan, Gilles Lubineau *

King Abdullah University of Science and Technology (KAUST), Physical Science and Engineering Division, COHMAS Laboratory, Thuwal, 23955-6900, Saudi Arabia

ARTICLE INFO

Keywords:
Damage mechanics
Delamination
Fibre bridging
Transverse cracking

ABSTRACT

Proper modeling of the interplay between transverse cracks and delamination is crucial in accurately simulating degradation in laminated composites. However, up to now, there is no computationally friendly model to account for this intra/inter laminar coupling. In this paper, a new hybrid cohesive law has been proposed in which the damage could be activated by both out-of-plane separation and in-plane strains of the interlaminar interface. By doing so, the in-plane strain can be used to estimate the damage state of the adjacent plies to the interface, so the response of the cohesive element is modified accordingly. This provides an efficient framework to account for the effect of intralaminar transverse cracks onto the delamination resistance. Through the authors' earlier work, the influence of intralaminar damage on interlaminar properties is twofold: harmful (through transverse crack-induced delamination) or beneficial (transverse crack-induced bridging). Both coupling effects are embedded in the hybrid cohesive elements. The modeling parameters are calibrated using rigorous experimental data. The simulation results demonstrate the potential of the pragmatic cohesive element proposed in this paper.

1. Introduction

Laminated composites, which are made by stacking unidirectional plies reinforced by continuous fibers, are an essential material in the design of lightweight structures in the automotive and aeronautical industries. Degradation modes of these materials are well known, ranging from fiber breakage, matrix yielding, micro-cracking, transverse cracks up to local and global delamination [1]. An accurate prediction of these mechanisms is then essential to the optimal use of these materials since the dominant failure mechanism could vary in different loading condition, stack sequence and material properties [2,3]. Through changing the staking sequence to an unbalanced laminate $[0/30]_{2s}$, the edge delamination could even occur before matrix cracking due to the reason that the shear stress is dominant in this off-axis layers [3]. One of the most challenging tasks is accurately predicting how mechanisms interact one to another. A well-known example is the coupling between intralaminar damage (that takes place in the unidirectional ply, such as fiber/matrix debonding or transverse cracking) and interlaminar damage (*i.e.,* delamination) [4–6]. These intra/inter coupling mechanisms can be harmful (through transverse crack-induced delamination) or beneficial (transverse crack-induced bridging). These two mechanisms are described further in the next two paragraphs.

The nucleation of local delamination in case of the saturation of transverse cracking [7–9] can significantly change the damage evolution process by degrading the interfacial properties. Although this mechanism has been extensively studied at different scales for the past twenty years, it is still challenging to account for it in a pragmatic modeling framework that would also result in efficient computations [10,11]. To the authors' knowledge, the literature today provides two main paths forward for the prediction of damage evolution in laminated composite, which are the explicit methods and the implicit methods or referred as smeared damage model in some research [2,12]. A review paper from Daum et al. [2] summarizes the computational approaches for predicting damage evolution, including semi-analytical model, explicit micro-models and multiscale models.

The first path widely used for the coupling study is to explicitly discretize the transverse cracks inside the composites. Different methods have been used in the literature, including the extended finite element method (XFEM) [13,14], the floating node method (FNM) [15–17], and the introduction of intralaminar cohesive elements inside plies [11,18]. The essential point is that the displacement jump and stress singularity due to the transverse crack are explicitly represented for all these methods. XFEM introduces an enriched shape function and extra degrees of freedom to depict the discontinuity displacement near a crack [19,

* Corresponding author.
E-mail address: gilles.lubineau@kaust.edu.sa (G. Lubineau).

https://doi.org/10.1016/j.compscitech.2020.108460
Received 18 May 2020; Received in revised form 2 September 2020; Accepted 9 September 2020
Available online 20 September 2020
0266-3538/

20], while FNM models discontinuity by introducing floating nodes to split the original element into sub-elements. These methods can give an accurate description of the out-of-plane stresses caused by transverse cracks. However, they require a refined mesh, and the meshing could be cumbersome due to the complex geometry. The second path is to homogenize this coupling using continuum damage mechanics [21]. The stress field in the ply is homogenized. During the homogenization, perturbations and stress singularities due to the transverse cracks have vanished as they correspond to a zero-mean-field at the mesoscale. This leads to a difficulty in accounting for the effect of transverse cracking on delamination at the mesoscale as the out-of-plane stress concentration inside plies, *i.e.,* the main driving force for creating local delamination, is filtered. As a way to introduce an adequate surrogate approach, a non-local damage model has been proposed to add an artificial coupling effect [22–24]. In this model, the interfacial interlaminar damage is not only affected by the damage state at that interface element itself, but it is also influenced by damage state or cracking densities of the adjacent plies. An appropriate internal variable is introduced to describe the transverse cracking density inside the ply. Then, the damage evolution law of the interface is parametrized by the level of transverse cracking. We stress that contrary to the approach we will propose in this paper, the damage is only triggered by out-of-plane stresses within the mesoscale cohesive element [22]. Such a non-local approach is not straightforward and intrusive to implement in commercial finite element code when the database is not fully opened as in ABAQUS, for example. It requires to write out damage variables of all integration points of plies from the previously converged step [23] to an external database. Then this database will be used to perform a non-local coupling for the current step. This results in an approximated time-discretization scheme, in between implicit and explicit, that is not very satisfactory from a convergence point of view.

In addition to the transverse crack-induced delamination (TCID), another coupling mechanism has been found in our previous study, which is referred to as transverse crack-induced bridging (TCIB) [25]. The experimental results in Ref. [25] revealed that the initiation of transverse cracks inside 90° plies promotes the fiber bridging in the transverse direction over the interface. As a result, the effective interface toughness increases as transverse crack density increases. Therefore, it is important to note that the transverse crack density will decide not only local delamination damage but also the extent of transverse bridging. To represent the bridging effect in cohesive element, a trilinear [26,27] or exponential [28] cohesive zone model (CZM) is usually adopted to mimic the R-curve. However, in the case of transverse cracks-induced bridging, the transverse bridging initiates from the beginning and does not result in a large process zone (contrary to the case of longitudinal bridging in which longitudinal fibers create long distance interactions and then an appreciable process zone). Therefore, we choose the traditional bilinear CZM [29] to embed both the coupling effect for modeling simplicity.

In this paper, both the transverse crack-induced delamination and bridging are embedded into a hybrid cohesive element. The hybrid cohesive element not only considers out-of-plane separation (as it is done for any cohesive interface) but also considers the in-plane strain of the interface, which serves as an indicator of the adjacent plies' intralaminar damage state. The coupling effect is implemented through a local approach instead of a non-local method. Thus, this hybrid cohesive element is non-intrusive and easy to be implemented into a commercial FE software - *i.e.,* ABAQUS.

The next section gives a brief description of the experimental results from the authors' earlier work on the influence of intralaminar damage on interlaminar properties. Section 3 presents the hybrid cohesive zone model and how we build it in the user subroutine (UEL) in ABAQUS. Section 4 shows the CAE model and simulation results, which match the experimental data well. Section 5 concludes this work with remarks on the performance of the hybrid cohesive element.

2. Experimental results

Referring to the work presented in Ref. [25], the authors implement a two-step experimental test to study the influence of intralaminar damage on the interlaminar performance (Fig. 1). The laminates in this experiment are manufactured from carbon fiber/epoxy prepregs (HexPly T700/M21, Hexcel) that are stacked by hand to create $[0_2/90_2]_s$ and $[0_6]$ stacking sequences. The fiber volume fraction of this prepreg is 57% and the thickness of each ply is 250 μm. The laminates are cured in a hydraulic hot-press machine (Pinette Emidecau Industries 15T) (7 bar pressure), and heated up to 180°C (heating rate: 2°C/min). The plates are remained at 180°C for 2 h and then cooled down to room temperature at a cooling rate of 3°C/min. First, tensile tests are carried out on the cross-ply samples $[0_2/90_2]_s$ with different in-plane strain levels. Then, we bond a backing adherend $[0_6]$ on each side of the tensile samples using Araldite 420 to provide enough bending stiffness so that subsequent DCB tests can be performed. Finally, we operate DCB tests on the back-bonded samples with different pre-defined levels of intralaminar damage. For each sample, the pre-defined intralaminar damage is quantified by the observed transverse cracking density in the 90° plies after in-plane extension. From the subsequent DCB test, the resulting interlaminar toughness during propagation, G_C, can be measured using the compliance calibration (CC) method [30]. Note that the back-bonded DCB samples $[0_6||0_2/90_2]_s$ are not strictly following the ASTM standard [30] since the delamination crack will occur and jump between the two 0/90 interface. An extra mesoscale FE simulation has been performed with the same configuration as the experimental samples, and the results have shown that the mode I dissipated energy G_{IC} represents around 90% percent of the whole energy dissipation. Thus, it is a valid method to evaluate the mode I behavior using the back-bonded DCB samples. Another remark should be made concerning the influence of transverse cracks on the overall stiffness. In fact, the 90-degree-ply contribution to the overall stiffness of cross-ply sample is small. An accurate prediction of stiffness reduction is mainly needed in the case of angle ply laminates including thick 90-degree plies or in the case of thermoplastic materials due to a much lower contrast in material properties [31]. This research focused on the influence of transverse cracks on the interface performance, which could induce transverse bridging and local delamination. Thus, the ply-stiffness degradation due to the transverse cracks does not play an significant role in the coupling mechanism.

Fig. 1 presents the experimental results of the evolution of transverse crack density and propagation G_C with respect to applied in-plane strain [25]. The propagation G_C is quite scattered, which is due to the randomness of the fiber bridging mechanism. Despite this, we can still observe a clear trend on how the propagation G_C evolves with respect to the applied in-plane strain level. The red circle and blue dot are from experimental data, while the red and blue solid lines are fitting these points. The average value of the propagation G_C is around 0.97 N/mm when the in-plane strain is lower than 0.2%. When the transverse crack initiated (in-plane strain above 0.2%), the propagation G_C started to increase (due to the transverse-cracks-induced bridging discussed in our previous work [25]). The propagation G_C keeps rising with the increase of transverse crack density and reaches the highest value around the in-plane strain of 0.8%. With a further increase of the in-plane strain of 0.8%, the transverse crack density saturates. Thus, the transverse cracks-induced bridging effect also gets saturated. In the meantime, local delamination starts to develop. Therefore, the propagation G_C shows a decreasing trend from 0.8% to 1.4%.

3. Pragmatic cohesive element

The experimental results described above illustrate a situation in which the mechanical performance of the interlaminar interface at the mesoscale is highly dependent on the level of transverse cracking in the adjacent plies. To design an appropriate cohesive element, we should

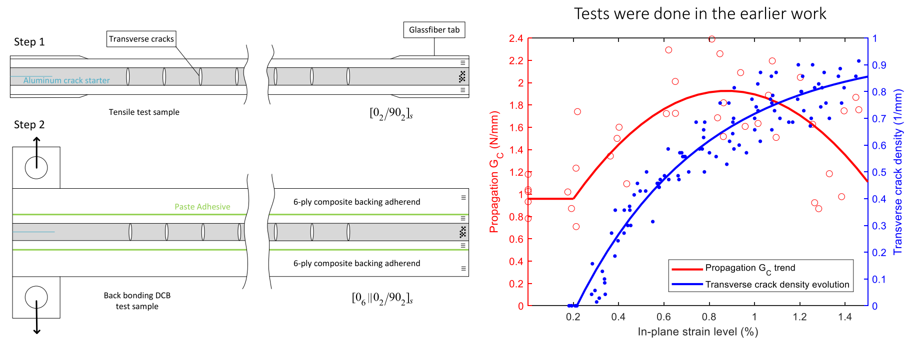

Fig. 1. Experimental results of the evolution of transverse crack density and propagation G_C[25].

first be able to estimate the density of transverse cracks in each ply and then account for this density of cracks within the cohesive zone model. This is done in the past by designing a non-local model coupling intra and interlaminar damage [22]. However, this approach is complicated and not practical for all the reasons cited in the introduction. Looking for a pragmatic approach will naturally drive us to a hybrid cohesive element, the damage of which being guided by both in-plane strain and out-of-plane separation. Indeed, while classical delamination is mainly dependent on out-of-plane stresses, the density of cracks in adjacent plies is mainly guided by the in-plane membrane-like loading.

3.1. Transverse crack density estimation

3.1.1. The classical approach

Earlier work by Lubineau and Ladevèze [23] specifically focus on describing at the mesoscale intralaminar damage. They decompose matrix damage into two-parts: one is diffuse matrix damage (that can be naturally homogenized as it is considered to be uniform within the thickness of the ply), and the other is transverse-cracking damage, for which they are able to obtain homogenized evolution laws using the so-called micro-meso relations [32,33]. In the following sections, $1, 2, 3$ represent the following: the fibers direction, transverse direction in-the-plane of ply, and the transverse direction out-of-the-plane of ply, respectively.

Let us recall the following damage evolution law that Lubineau and Ladevèze proposed for the evolution of transverse cracking density within the single ply Eq. (1) [23]. This evolution law is based on the thermodynamics forces Y_{22}^{tc}, Y_{12}^{tc}, Y_{23}^{tc} associated with the multiplication of transverse cracks in each mode:

$$\left[\left(\frac{Y_{22}^{tc}\frac{\partial d_{22}^{tc}}{\partial \rho}}{G_{IC}}\right)^{\alpha}+\left(\frac{Y_{12}^{tc}\frac{\partial d_{12}^{tc}}{\partial \rho}}{G_{IIC}}\right)^{\alpha}+\left(\frac{Y_{23}^{tc}\frac{\partial d_{23}^{tc}}{\partial \rho}}{G_{IIIC}}\right)^{\alpha}\right]^{\frac{1}{\alpha}}=1 \qquad (1)$$

where d_{22}^{tc}, d_{12}^{tc} and d_{23}^{tc} are the damage variable that quantify the effect of transverse cracks on the homogenized stiffness of the mesoscale ply. The relationship between d_{22}^{tc}, d_{12}^{tc}, d_{23}^{tc} and ρ are obtained by homogenization simulation using micro-meso relations [32,33]. Thus the three damage variables d_{22}^{tc}, d_{12}^{tc}, d_{23}^{tc} are not independent. G_{IC}, G_{IIC} and G_{IIIC} are the toughness corresponding to the respective fracture modes. Y_{22}^{tc}, Y_{12}^{tc}, Y_{23}^{tc} are calculated as follows [32,33]:

$$\begin{aligned}
Y_{22}^{tc} &= H\left[\frac{\langle\sigma_{22}\rangle_+^2}{2E_2^0\left(1-d_{22}^{tc}\right)^2\left(1-d_{22}^{diff}\right)}-\frac{\nu_{23}^0\sigma_{33}\langle\sigma_{22}\rangle_+}{E_2^0\left(1-d_{22}^{tc}\right)^2}\right]\\
Y_{12}^{tc} &= H\left[\frac{\sigma_{12}^2}{2G_{12}^0\left(1-d_{12}^{tc}\right)^2\left(1-d_{12}^{diff}\right)}\right]\\
Y_{23}^{tc} &= H\left[\frac{\sigma_{23}^2}{2G_{23}^0\left(1-d_{23}^{tc}\right)^2\left(1-d_{23}^{diff}\right)}\right]
\end{aligned} \qquad (2)$$

where $\langle x\rangle_+ = 0$ if $x \le 0$, $\langle x\rangle_+ = x$ if $x > 0$. d_{22}^{diff}, d_{12}^{diff} and d_{23}^{diff} are the diffuse damage variables, corresponding to the debonding of the fiber/matrix interface that is homogeneously distributed within the thickness of the ply at the mesoscale. H denotes the thickness of the ply.

Calculating the density of transverse cracks using these equations at the mesoscale is always challenging as they are essentially non-local. Indeed, the damage force is based on average quantities over the thickness of the ply [21]. This is difficult to handle in commercial platforms such as ABAQUS, because the database is structured around the elementary integration point. That means that when integrating at the level of a specific integration point, data about state variables at other locations are not steadily available. Due to this, specific computation schemes have been proposed [23] in which information is stored in a temporary buffer and calculations are in between implicit and explicit. This is, of course, not fully satisfactory, both from a computation efficiency and from a convergence control standpoint. The problem becomes even more severe when calculating a ply-dependent interface. Indeed, when calculating the interface element, accessing the updated ply state variable (typically the level of transverse cracking) is challenging.

This is the point of the current publication: simplifying this process by the development of a new type of hybrid cohesive element.

3.1.2. Towards a simplified approach

The first modeling choice to achieve this required simplification is to ignore the effect of out-of-plane stress on transverse cracking. This is reasonable as transverse cracks are in practical configurations mainly activated by shear and transverse in-plane loadings.

The second choice is to use the value of damage force at the initiation of damage. Even though this is a coarse approximation, it provides a fair estimation of mode mix, and ensures a rapid estimation that is deemed enough to predict the evolution of the interface due to this damage. All the damage variables, *i.e.*, d_{22}^{tc}, d_{12}^{tc} and d_{23}^{tc}, are all 0 at the beginning of transverse cracking. The diffuse damage variable could be assumed as 0, also, since the diffuse damage level is always very limited in systems exhibiting a lot of transverse cracks. In this case, Y_{22}^{tc}, Y_{12}^{tc} and Y_{23}^{tc} could be simplified as follows:

$$Y_{22}^{tc} = H\left[\frac{\langle\sigma_{22}\rangle_+^2}{2E_2^0}\right]$$
$$Y_{12}^{tc} = H\left[\frac{\sigma_{12}^2}{2G_{12}^0}\right] = H\frac{G_{12}^0\varepsilon_{12}^2}{2} \tag{3}$$
$$Y_{23}^{tc} = 0$$

σ_{22} is obviously a function of ε_{11}, ε_{22} and ε_{12}, so we can obtain a damage force only formulated as a function of the in-plane strain of the ply.

At this point, we now note that the in-plane strain of the mesoscale ply is very close to the in-plane strain of its adjacent interface if the laminate experiences limited bending. This is generally the case in composite structures. The main idea is then to develop a hybrid interface element, in which the in-plane part of the strain, that is usually ignored, and this can be used to predict the level of crack density in the adjacent plies.

3.2. A hybrid cohesive element

Fig. 2 shows the schematic of a 3D 8-node cohesive element. For classical cohesive element, only the out-of-plane separation is considered. The separation (displacement jump) is obtained and used to calculate the traction of the crack surface based on the pre-defined traction-separation law. However, in this paper, we will develop a hybrid novel cohesive element in which the in-plane strains at the top and bottom surfaces of the cohesive element are also playing a role in the calculations of the cohesive tractions.

As shown in Fig. 2, the separation is based on the local coordinates system of the middle plane of the cohesive element. The global coordinate system of the cohesive element's node is used to determine the normal direction n to the middle plane surface and two orthogonal in-plane direction s and t. The separation is then defined as the displacement difference of top surface node $1,2,3,4$ and bottom surface node $5,6,7,8$, as seen in Eq. (4). δ_s^{mi} and δ_t^{mi} are the shear-mode separations of node mi in the middle surface. δ_n^{mi} is the normal mode separation of node mi in the middle surface. u_n^i, u_s^i and u_t^i denote the displacement of element node i in the element local coordinate system n, s, and t, respectively. Meanwhile, the strain is defined using the displacement field interpolated by the displacement of element node $1,2,3,4$ and $5,6,7,8$, as seen in Eq. (5). The calculated in-plane strains are then transformed to the material direction 1, 2, and 3, of the top and bottom plies, which provide a fair estimation of the in-plane strain in the adjacent plies and also the transverse crack densities. By doing so, the response of cohesive element can be modified to account for the damage in adjacent plies.

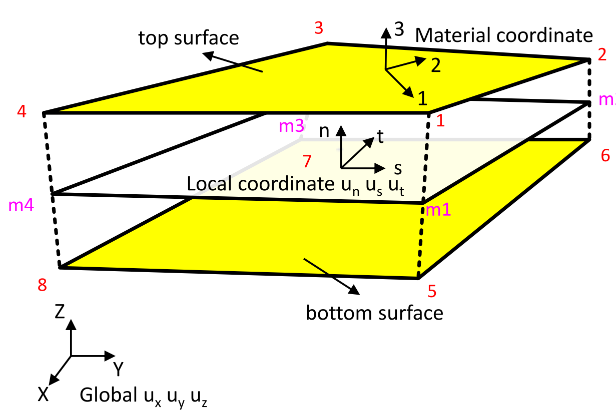

Fig. 2. Schematic of a 8-node cohesive element giving the information of out-of-plane separation and in-plane strain.

$$\underline{\delta} = (\delta_n, \delta_s, \delta_t)^T = \begin{cases} \delta_n^{mi} = u_n^i - u_n^{i+4} \\ \delta_s^{mi} = u_s^i - u_s^{i+4}, i = 1,2,3,4 \\ \delta_t^{mi} = u_t^i - u_t^{i+4} \end{cases} \tag{4}$$

$$\varepsilon_{ij} = \frac{1}{2}\left(\frac{\partial u_i}{\partial x_j} + \frac{\partial u_j}{\partial x_i}\right) i,j = s,t \qquad \varepsilon_{ss}, \varepsilon_{st}, \varepsilon_{tt} \Rightarrow \varepsilon_{11}, \varepsilon_{12}, \varepsilon_{22} \tag{5}$$

The coupling mechanism is decomposed into transverse crack-induced bridging and transverse crack-induced delamination as presented in the experimental work in Ref. [25]. A critical strain (here identified to be 0.8% for our material) is set as the threshold where local delamination will occur. This is in practice the in-plane strain at which transverse crack density starts to get saturated. Therefore, from in-plane strain of 0.2% to 0.8%, only the TCIB is triggered. While from in-plane strain of 0.8% to 1.4%, both TCIB and TCID mechanisms are triggered. The following sections will explain in detail about how we embed the two coupling mechanisms in a classical bilinear BK cohesive model.

3.2.1. Classical bilinear BK cohesive zone model

Eq. (6) gives the constitutive equation of a classical cohesive zone model. τ is the element traction, and δ is the separation. τ_s and τ_t represent the shear traction corresponding to mode II and mode III fracture, and τ_n represents the out-of-plane transverse traction corresponding to mode I fracture. K is the initial stiffness, which is usually assigned a very large value to avoid spurious compliance due to the introduction of cohesive elements. K is the same for all three separation directions, and an isotropic damage d is assumed.

$$\begin{bmatrix}\tau_s\\ \tau_t\\ \tau_n\end{bmatrix} = \begin{pmatrix}(1-d)K & 0 & 0\\ 0 & (1-d)K & 0\\ 0 & 0 & (1-d)K + dK\frac{\langle -\delta_n\rangle}{\delta_n}\end{pmatrix}\begin{bmatrix}\delta_s\\ \delta_t\\ \delta_n\end{bmatrix} \tag{6}$$

For a bilinear cohesive zone model, the damage is defined by the current maximum separation $\delta_m^{\max}$, the separation for damage initiation δ_m^0, and the separation for failure δ_m^f, as shown in Eq. (7) [29]. The mix mode separation is defined as in Eq. (8), where $\langle x\rangle = x$, when $x \geq 0$ and $\langle x\rangle = 0$,when $x < 0$. The maximum separation $\delta_m^{\max}$ is stored in a state variable in the UEL [34] and compared with the current mixed separation to choose the larger one.

$$d = \frac{\delta_m^f\langle\delta_m^{\max} - \delta_m^0\rangle}{\delta_m^{\max}(\delta_m^f - \delta_m^0)} \tag{7}$$

$$\delta_m = \sqrt{\delta_s^2 + \delta_t^2 + \langle\delta_n\rangle^2} \tag{8}$$

In this paper, a quadratic damage initiation and BK mixed mode propagation criterion are adopted [29,35,36] to define the δ_m^0 and δ_m^f, as shown in Eq. (9) and Eq. (10). τ_s^0, τ_t^0, and τ_n^0 are the traction for damage initiation in mode II, III and I, respectively. G_{IC} and G_{IIC} are the critical energy release rate for mode I and mode II. η is a parameter obtained from mixed mode bend (MMB) tests at different mixed mode ratios β, which is only defined when $\delta_3 > 0$. Otherwise, only the shear interface damage is triggered.

$$\left(\frac{\langle\tau_n\rangle}{\tau_n^0}\right)^2 + \left(\frac{\tau_s}{\tau_s^0}\right)^2 + \left(\frac{\tau_t}{\tau_t^0}\right)^2 = 1 \tag{9}$$

$$G_{IC} + (G_{IIC} - G_{IC})\left(\frac{G_{shear}}{G_T}\right)^\eta = G_C \qquad G_{shear} = G_{II} + G_{III}, G_T = G_I + G_{shear} \tag{10}$$

$$\beta = \frac{\delta_{shear}}{\delta_n} = \frac{\sqrt{\delta_s^2 + \delta_t^2}}{\delta_n} \tag{11}$$

Therefore, we can deduce the formulation of δ_m^0 and δ_m^f:

$$\delta_m^0 = \begin{cases} \delta_n^0 \delta_s^0 \sqrt{\dfrac{1+\beta^2}{\left(\delta_s^0\right)^2 + \left(\beta \delta_n^0\right)^2}}, \delta_n > 0 \\ \delta_{shear}^0 = \delta_s^0, \delta_n \leq 0 \end{cases} \tag{12}$$

$$\delta_m^f = \begin{cases} \dfrac{2}{K\delta_m^0}\left[G_{IC} + (G_{IIC} - G_{IC})\left(\dfrac{\beta^2}{1+\beta^2}\right)^{\eta}\right], \delta_n > 0 \\ \delta_s^f, \delta_n \leq 0 \end{cases} \tag{13}$$

3.2.2. Pragmatic cohesive zone model

To account for the transverse crack-induced bridging contribution in the classical linear BK law, we will make the G_{IC} dependent on the history of the applied in-plane strain. The experimental results in the authors' earlier work [25] show that more transverse bridging is triggered with the increase of the transverse crack density in the 90° plies. As explained in subsection 3.1, the transverse crack density of the 90° plies can be estimated by the in-plane strain of the cohesive element. Therefore, we will build a relationship between the total dissipated energy during delamination and in-plane strain, as shown in Eq. (14).

$$G_C^{bridg} = f(\rho) = g\left(max(\varepsilon_{22})|_t, max(\varepsilon_{12})|_t\right) \tag{14}$$

Eq. (14) is a general formulation that indicates the role of both shear and transverse in-plane components to the development of transverse cracks. This general relation can be for example calculated based on the micro-meso relationships derived by Ladevèze and Lubineau in Ref. [23]. In the current work, we are willing to provide a proof of concept and restrict ourselves to the simple configuration described in section 2. Only transverse strains are then considered, and the total dissipated energy during delamination with bridging G_C^{bridg} becomes directly the input G_{IC} in Eq. (13). Thus, the separation for failure δ_m^f is dependent on the maximum applied in-plane strain over history. G_C^{bridg} is calibrated from the experimental data in Fig. 3 from in-plane strain of 0.2% to 0.8%.

In the second stage from in-plane strain of 0.8% to 1.4%, the increasing rate of G_C^{bridg} slows down due to the saturation of transverse crack density. Meanwhile, the effective G_C starts to decrease due to the transverse crack-induced delamination. The presence of local delamination decreases the effective area of interlaminar interface, as shown in the green area in Fig. 3. We modify the damage variable in Eq. (6) to account for this influence:

$$d = 1 - \left(1 - \frac{\delta_m^f \langle \delta_m^{max} - \delta_m^0 \rangle}{\delta_m^{max}\left(\delta_m^f - \delta_m^0\right)}\right)(1 - d_{TCID}) \tag{15}$$

where d_{TCID} denotes the damage caused by transverse crack-induced delamination. d_{TCID} will be calibrated using the experimental data in Fig. 3 from in-plane strain of 0.8% to 1.4%. The following subsection will explain in detail about the calibration of G_C^{bridg} and d_{TCID}.

In the end, both coupling mechanisms will change the damage evolution of the pragmatic cohesive zone model. The transverse crack induced-bridging modifies the total dissipation energy with bridging G_C^{bridg} and lead to a different failure separation δ_m^f. At the same time the transverse crack-induced delamination adds one more part d_{TCID} in the final damage evolution.

Fig. 4 illustrates how the two coupling mechanisms reshape the traction separation law. For low in-plane strain (0% and 0.2%), the traction separation law is the same since no transverse crack initiated. When transverse cracks start to appear (around 0.2% strain), the separation for failure δ_m^f increases, which corresponds to additional

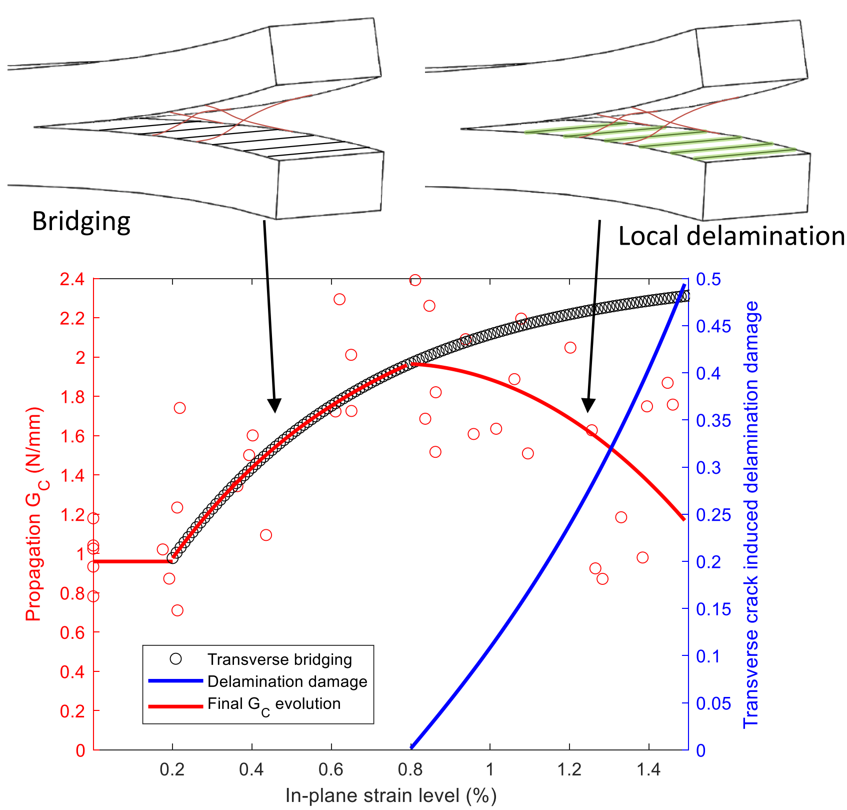

Fig. 3. Parameters calibration of the bridging effect and local delamination effect.

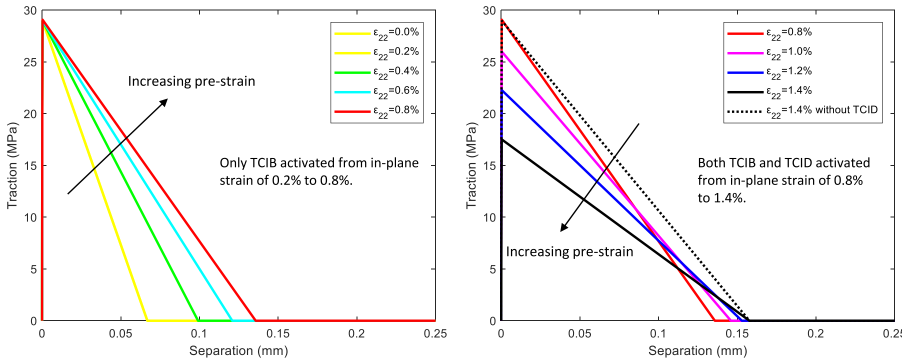

Fig. 4. Schematic of the pragmatic cohesive zone model.

dissipation of energy inherited from fiber bridging (Fig. 4, left). For cases with higher in-plane strain of 0.8% (Fig. 4, right), the failure separation δ_m^f is still increasing with the increasing in-plane strain but at a slower rate because of the saturation of the transverse crack density. In the meantime, the transverse crack-induced delamination damage d_{TCID} starts to increase, which decreases the total dissipated energy. The black dot line in Fig. 4 shows the traction separation law without TCID included, which has much more energy dissipated compared to the black straight line (with both TCIB and TCID considered).

3.2.3. Calibration of parameters and UEL flowchart

An exponential function is adopted to describe the G_C^{bridg} evolution with respect to in-plane strain, as seen in Eq. (16). The random defects inside the 90° plies help to trigger transverse bridging. Thus, the G_C^{bridg} increases sharply from 0.2% when the first transverse cracks appear and the increase rate slows down with the saturation of transverse crack after 0.8%. G_{ini} corresponds to the effective G_C when the maximum in-plane strain ε_{22}^{max} is lower than 0.2%, which is the case with very limited transverse bridging. From the in-plane strain of 0.8% to 1.4%, local delamination damage is triggered. The two coupling mechanisms TCIB and TCID start to compete with each other. We use a superposition of two exponential functions, as seen in Eq. (17) to account for the TCID evolution. d_{TCID} equals to 0 when the maximum in-plane strain is lower than 0.8%. The current maximum in-plane strain ε_{22}^{max} is defined as the larger one of the current maximum in-plane strain of the top and bottom surface $\varepsilon_{22}^{top,max}$ and $\varepsilon_{22}^{bottom,max}$, as shown in Eq. (18).

In Fig. 3, the black circle is the G_C^{bridg} evolution while the solid blue line is the TCID evolution. The superposition of the two coupling mechanisms gives the final effective propagation G_C evolution, which is shown with the solid red line. Thus, the calibration for the coupling parameters follows two steps. The experimental toughness between in-plane strain of 0.2% and 0.8% is first used to calibrate the coupling parameters for G_C^{bridg}, *i.e.,* a_1, a_2, a_3, and a_4. In the second step, the d_{TCID} parameters are calibrated using the difference between experimental toughness evolution and the G_C^{bridg} evolution. Table 1 presents all the coupling parameters in this pragmatic cohesive model. The initial toughness is 0.97 N/mm when the preset in-plane strain is lower than 0.2%. The Mode II toughness used in this work is set as 1.79 N/mm, which is a common value adopted in literature for the material of T700/M21 [37]. τ_n^0 and τ_s^0 are two simulation parameters, which are set as 29 MPa and 40 MPa, respectively.

Table 1
Coupling parameters for the pragmatic cohesive model.

a_1	a_2	a_3	a_4	b_1	b_2	b_3	b_4
−2.77	−1.89	−0.26	2.44	0.044	1.71	−0.42	−1.08
G_{ini}	G_{IIC}	τ_n^0	τ_s^0				
0.97 N/mm	1.79 N/mm	29 MPa	40 MPa				

Note that the two-step test for calibration of the coupling parameters is based on the specific configuration of $[0_6||0_2/90_2]_s$ within a mode I fracture behavior. With different ply orientation, thickness of the plies with matrix cracks, and loading condition, the coupling parameters could be different since the TCIB is a non-local structural effect which depends on the extrinsic conditions. We intend to include these factors for a more general coupling modeling in the future.

$$G_C^{bridg} = \begin{cases} a_1 e^{a_2 \varepsilon_{22}^{max} + a_3} + a_4, \varepsilon_{22}^{max} \geq 0.2\% \\ G_{ini}, \varepsilon_{22}^{max} < 0.2\% \end{cases} \quad (16)$$

$$d_{TCID} = \begin{cases} b_1 e^{b_2 \varepsilon_{22}^{max}} + b_3 e^{b_4 \varepsilon_{22}^{max}}, \varepsilon_{22}^{max} \geq 0.8\% \\ 0, \varepsilon_{22}^{max} < 0.8\% \end{cases} \quad (17)$$

$$\varepsilon_{22}^{max} = max\left\{\varepsilon_{22}^{top,max}, \varepsilon_{22}^{bottom,max}\right\} \quad (18)$$

To implement the pragmatic cohesive zone model, ABAQUS subroutine user defined element (UEL) [34] is adopted. Fig. 5 gives the flowchart of the implementation of the pragmatic CZM using UEL. ABAQUS provides input data such as the global coordinate and displacement information of the cohesive element nodes to the UEL, and the UEL provides output such as the element stiffness matrix and force vector. First, we transformed the global coordinate and global displacement of the cohesive element nodes to the local coordinates and local displacement in the material direction 1, 2, and 3. Once the local displacement of the nodes were found, we calculated the current separation and in-plane strain which can then be used to compare with the maximum separation and in-plane transverse strain stored in UEL state variables. We use the maximum in-plane strain ε_{22}^{max} to update the G_C^{bridg} and d_{TCID}. Finally, we can use the current maximum separation to calculate the interface damage and traction. As a result, we can update the stiffness matrix and force vector for ABAQUS calculation. To achieve a better convergence during the damage propagation, we provide the tangent constitutive tensor $\partial T_c/\partial \Delta$ instead of the secant constitutive stiffness. We adopt a numerical method to achieve the tangent stiffness matrix [38], which could be expressed as:

$$D_{ij}^T = \frac{\tau_i^{\delta_j + \Delta\delta_j} - \tau_i^{\delta_j}}{(\delta_j + \Delta\delta_j) - \delta_j}, i, j = 1, 2, 3 \quad (19)$$

where $\tau_i^{\delta_j}$ is the traction component associated with the separation δ_j. We choose a small value of 10^{-14} for $\Delta\delta_j$, so D_{ij}^T is a viable approximation of the real tangent stiffness.

3.3. Thermodynamic consistency of the pragmatic cohesive law

This section will discuss about the thermodynamic consistency of the

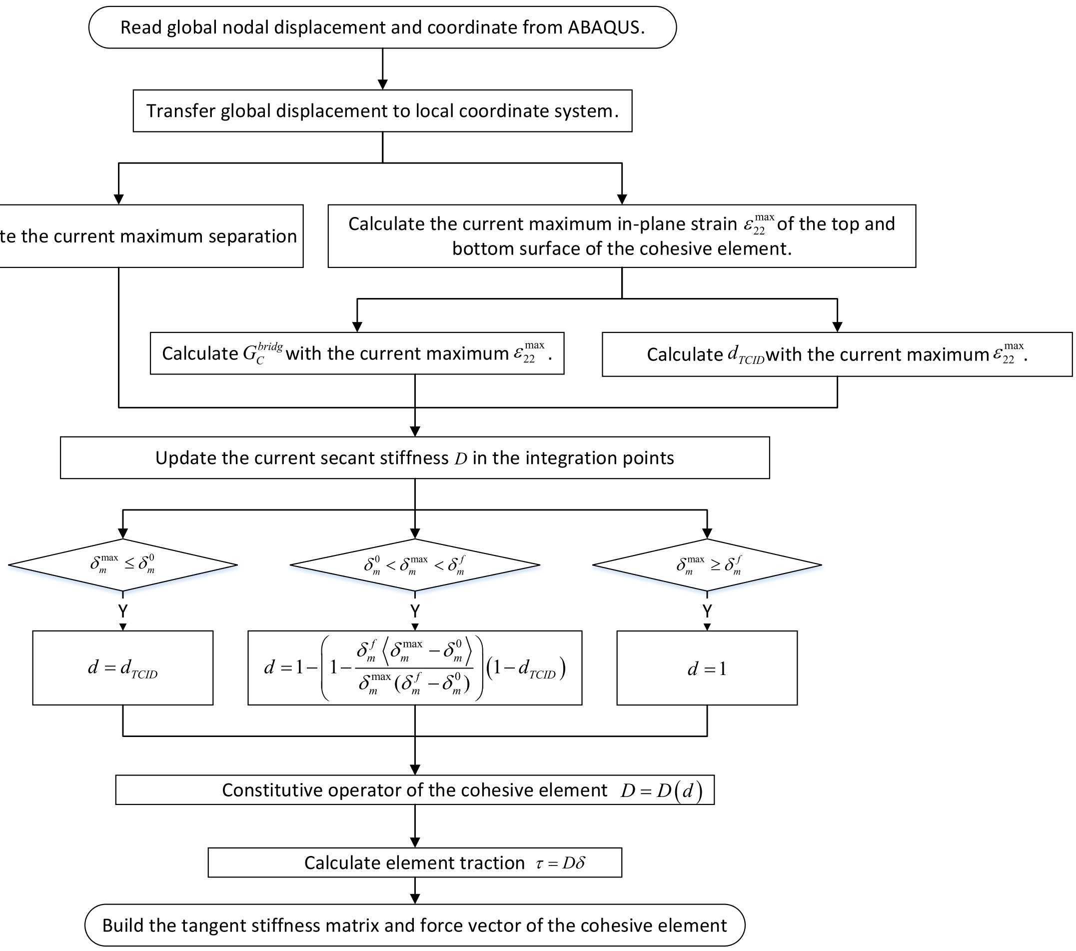

Fig. 5. Flow chart of the pragmatic cohesive element.

pragmatic cohesive law when complex loading path is applied on a single cohesive element. As shown in Fig. 6, Two kinds of loading are applied to a single cohesive element: in-plane strain and out-of-plane separation. The in-plane strain and normal separation are defined by prescribing directly the nodal displacements of the cohesive element (u_x of the eight nodes for the in-plane strain and u_z for the normal separation). By combining the sequence of the in-plane strain and normal separation, we can check the traction separation response under different loading path.

Three simple loading paths are shown in Fig. 7. For path1, we apply first a normal separation that fully damages the element, and an in-plain strain of 0.4% follows. For path3, we apply a preset in-plane strain of 0.4%, and the normal separation is applied afterwards. For path2, we follow a path in between path1 and path3, for which the in-plain strain is applied while the interface is not fully damaged. Path1 follows the original traction separation curve since the interface is already fully damaged when we apply the in-plane loading. Path3 fully activates the transverse crack-induced bridging energy since the interface property is modified before the normal separation. Path2 modifies the in-plane strain during the softening process of the original traction separation curve. At the transition point when $\delta_3 = 0.02$mm, the reaction force suddenly increases to the path3 curve since the toughness increases. The dissipated energy depends on the loading path in our pragmatic cohesive model because the transverse strain of the interface element is an indicator of the adjacent plies' damage state. It is obvious that the dissipated energy will be different when the in-plane strain is applied after the failure of cohesive element and before the out-of-plane loading. This is consistent with the physical mechanisms as bridging might be introduced or not depending on the loading path.

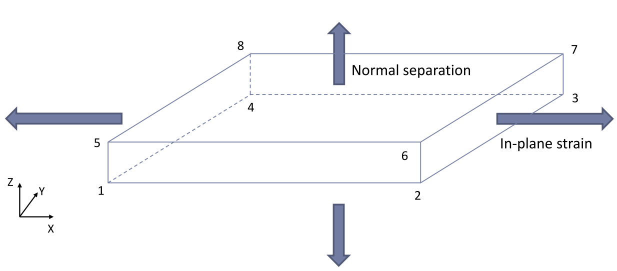

Fig. 6. Complex loading path on a single cohesive element.

Fig. 8 illustrates in detail how the traction-separation curve is dependent on the loading path. For path4, we increase the in-plane strain and normal separation simultaneously. When the separation increase to 0.05 mm, the in-plane strain reaches to 0.2%, which is the initiation threshold for the TCIB energy. Therefore, the toughness starts to increase at this transition point. The black dash line is the traction separation curve in case a 0.24% preset in-plane strain is applied. The black dash line intersect with the curve of path4 at the separation of 0.06 mm when the in-plane strain reaches to 0.24%. This evolution is of course path-dependent. As shown in Fig. 9, when the in-plane strain increases a little bit faster in path5, the transition point will occur earlier at $\delta_3 = 0.04$mm where ε_{22} reaches 0.2%. The toughness will stop increasing when the separation reaches 0.08 mm with the in-plane strain remaining 0.4%. Thus, the traction separation curve of path5 will follow path3 after δ_3 reaches to 0.08 mm.

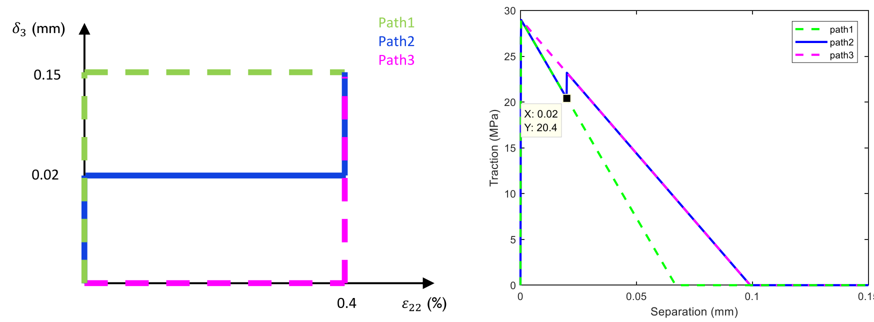

Fig. 7. Traction separation response under loading path1, path2, and path3.

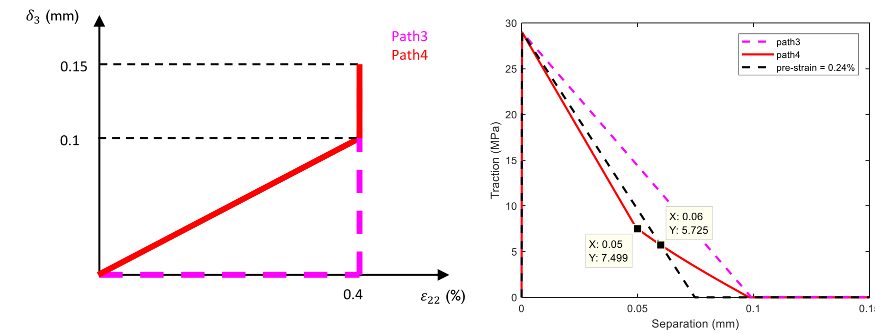

Fig. 8. Traction separation response under loading path3 and path4.

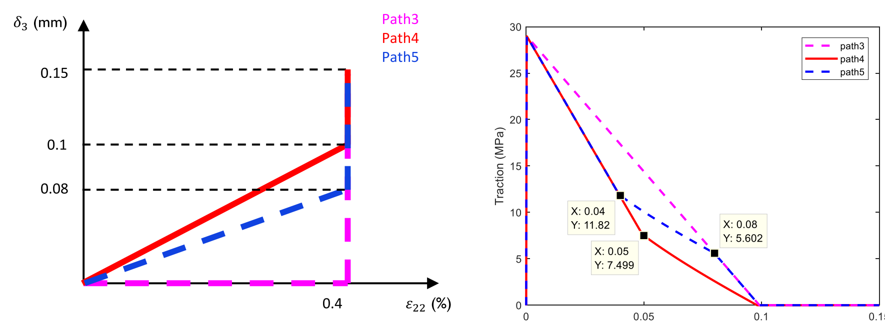

Fig. 9. Traction separation response under loading path3, path4, and path5.

4. Simulation results

In this part, we performed two types of simulations. The first is to validate the UEL by comparing it with the ABAQUS built-in model without taking into account the coupling effect. For this, we simulate the DCB response of a standard $[0_8]_s$ laminate. The second simulation is to validate the proposed hybrid CZM by comparing it with experimental results using our UEL (stacking sequence of $[0_8/90_2]_s$). The geometry of the model and the results will be discussed in detail in the following subsections.

4.1. Validation of UEL

The pragmatic cohesive element is developed as a user-defined element in ABAQUS (UEL) written as a Fortran subroutine. In this subsection, we validate our UEL by comparing it with ABAQUS built-in cohesive element. We performed a DCB simulation, using 8-node linear brick elements with reduced integration (C3D8R) for the DCB arm. The element size for the DCB model in this section is uniform as 0.5 mm. The interface was modeled by both ABAQUS built-in quadratic BK cohesive element (COH3D8) and our homemade UEL without coupling. The pre-crack length is 50 mm, with a total thickness of 4 mm. The simulation model width is 10 mm, which is half of the DCB sample. The elastic constants employed for the DCB arms are: $E_{11} = 135$ GPa, $E_{22} = E_{33} = 9.7$ GPa, $G_{12} = G_{13} = 5.3$ GPa, $G_{23} = 3.3$ GPa, $\nu_{12} = \nu_{13} = 0.32$ and $\nu_{23} = 0.487$. The mode I critical energy release rate G_{IC} in the model is 0.6 N/mm.

Fig. 10 shows the force-displacement curve with ABAQUS built-in cohesive element and our UEL. The yellow curve is the theoretical results based on Euler-Bernoulli beam theory. The result with ABAQUS built-in cohesive element matches well with the result using UEL. This work is aimed to check the finite element formulation of the UEL. Based on this validation, we can further develop the coupling strategy.

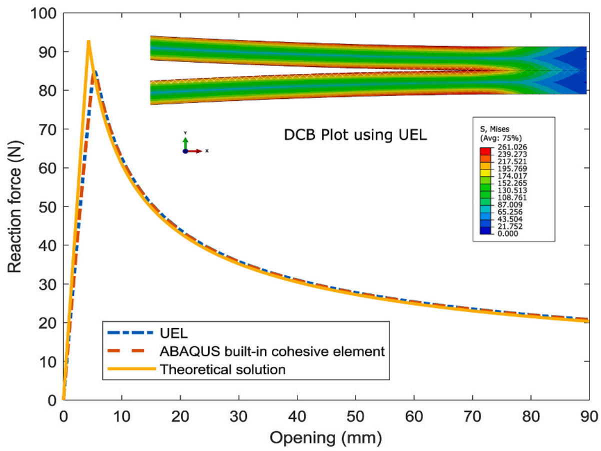

Fig. 10. Comparison of DCB simulation results using ABAQUS built-in cohesive element and UEL.

4.2. Computational model

In this section, the two-steps test (in-plane tensile loading followed by DCB loading) is simulated with a mesoscale model. Only half of the DCB sample is modeled due to its symmetry in the width direction. The geometry of the finite element model is shown in Fig. 11. The element size for the DCB model in this section is uniform as 0.5 mm. Elementary ply is 0.25 mm-thick. The dimensions of the model are 255 mm-long, 10 mm-wide, and 5 mm-thick, with a pre-crack of 55 mm-long. The stacking sequence of the sample is $[0_8/90_2]_s$. The DCB arm is modeled with 8-node linear elastic brick elements with reduced integration (C3D8R). The elastic constants employed for the DCB arms are: $E_{11} =$ 135 GPa, $E_{22} = E_{33} = 9.7$ GPa, $G_{12} = G_{13} = 5.3$ GPa, $G_{23} =$ 3.3 GPa, $\nu_{12} = \nu_{13} = 0.32$, and $\nu_{23} = 0.487$. The degradation of the interface is simulated with our hybrid cohesive element. The hybrid cohesive element will not only calculate the damage due to the local kinematic of the interface but also include the transverse crack-induced delamination and transverse crack-induced bridging due to the in-plane load history. The coupling parameters are calibrated with the experimental data in Fig. 3. Note that in this simulation, only one layer of interface elements is inserted at the 90/0 interface, as illustrate in Fig. 11. While migration/jump between the two 0/90 interface can be observed in the experiments, this is related to the contrast and randomness of the material properties, as recently observed from the examples of secondary adhesive bonding [39,40]. There is a further development to be done on our model in the future, which is to include the stochastic layer on top of the deterministic intra/inter coupling.

The boundary condition is applied in two steps, and symmetric boundary condition is applied on the middle surface S3 for both steps since only half of the sample is simulated. In the first step, tensile loading was applied on surface S1 and S2 with eight different strain levels ranging from 0% to 1.4%. We then unload the model to recover to the initial position. This step is used to record the in-plane loading history of the adjacent plies of the cohesive interface element. The maximum in-plane strain ε_{22}^{max} is then stored to modify the interlaminar properties of the cohesive elements, as illustrated in the flowchart Fig. 5. DCB boundary condition is applied in step 2, with $u_x = u_y = 0$ on line L2 and $u_x = 0$ on L1. u_y is progressively increased on line L1, and the maximum opening applied in the model is 90 mm.

4.3. Results

Fig. 12 shows a good agreement between the experimental and simulation results for the preset in-plane strains of 0%, 0.8%, 1.0%, and 1.4%. The comparison between 0.0% and 0.8% shows the increasing reaction force in the stage where only TCIB activated. For the comparison results between preset in-plane strain of 1.0% and 1.4%, both TCIB and TCID activate. However, the TCIB starts to saturated while the TCID increases exponentially. Thus, the reaction force of 1.4% decreases compared to 1.0% in the simulation results. Meanwhile, we observe that the experimental curve widely fluctuates due to the stochastic transverse fiber bridging, especially for the results of in-plane strain of 1.4%. In this case, althought TCID is fully developed, the reaction force could still remain high in some samples where the TCIB extensively yields. The simulation results are in the middle of the experimental curve because we use the averaged value of propagation G_C in the stable delamination propagation zone to calibrate our hybrid cohesive zone model.

Simulation results with different preset in-plane strains are presented in Fig. 13. Since there is no fiber bridging below 0.2% pre-strain, all results are identical and the pre-strain has no effect on the DCB result. Between 0.2% and 0.8% pre-strain, only transverse bridging is triggered. Therefore, the performance of the interface is improved due to the extensive development of fiber-bridging that is accurately accounted for in the model. From 0.8% to 1.4% in-plane strain, both transverse cracks induced bridging and delamination are triggered. However, due to the saturation of the intralaminar damage after the in-plane strain of 0.8%, the bridging effect also gets saturated. In this stage, the transverse crack-induced local delamination becomes the major governing mechanism that leads to the decrease of apparent fracture toughness (*i.e.,* the reaction force decreases as the preset in-plane strain increases from 0.8% to 1.4%.).

5. Conclusion

A novel hybrid cohesive element that considers the coupling effect between intralaminar damage and interlaminar damage has been successfully proposed in this paper. The damage state of the hybrid cohesive element is not only dependent on the local kinematic of the interface but also depends on the intralaminar damage of the adjacent plies. The intralaminar damage is represented by its transverse crack density, which is estimated by the in-plane strain of the surface of the hybrid cohesive element.

In this paper, we also include the influence of the transverse cracking-induced bridging, which initiates around 0.2% preset in-plane

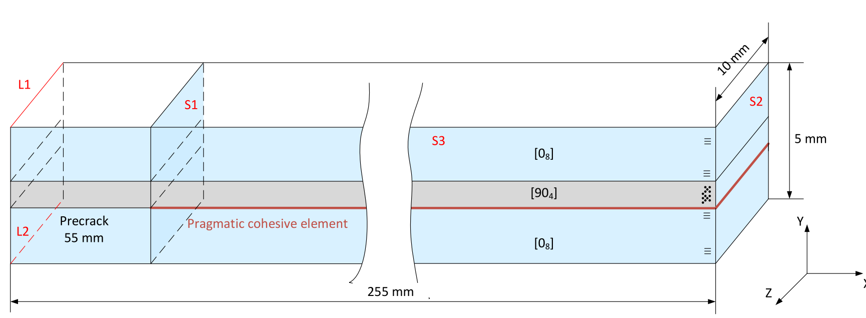

Fig. 11. CAE model configuration.

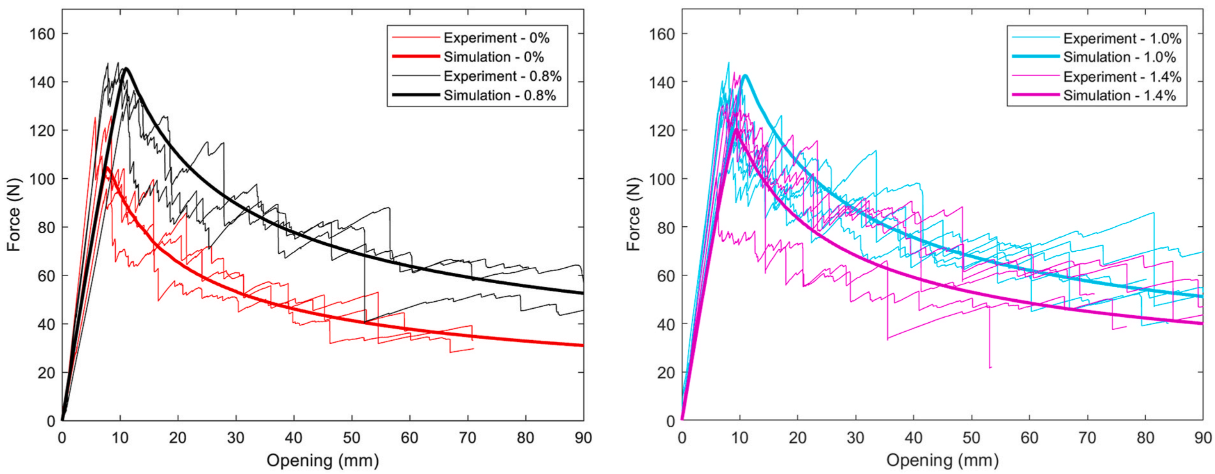

Fig. 12. Comparison of simulation results and experimental data.

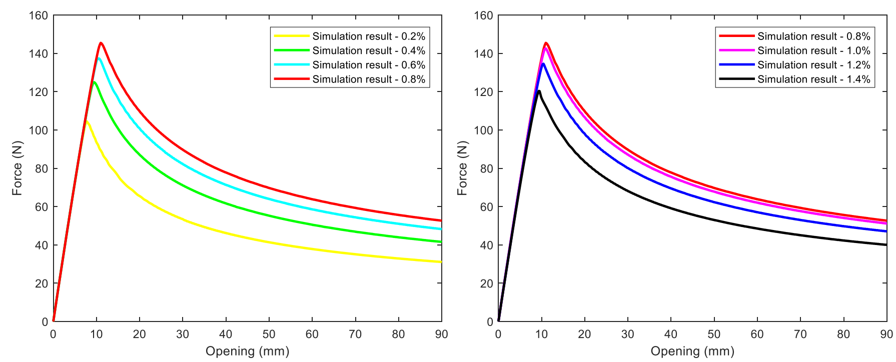

Fig. 13. Simulation results of P-δ curve with different preset in-plane strain.

strain. As the preset in-plane strain increases, the transverse crack density increases, and thus, the transverse bridging effect also increases exponentially. When transverse cracking reaches its saturation level (*i. e.,* for in-plane strain higher than 0.8%), the transverse crack-induced local delamination is triggered. Thus, beyond in-plane strain higher than 0.8%, strong competing mechanisms between transverse crack-induced bridging and local delamination govern the apparent toughness. We captured this behavior by using the traction-separation law that is tailored toward these competing mechanisms. Our future work will examine the quality of the proposed model in more complicated situations, such as in an open-hole tension, where the transverse cracks may influence the delamination mechanisms.

Additional information - competing interests

The authors declare no financial or non-financial competing interests.

Data availability

The datasets generated during and/or analyzed during the current study are available from the corresponding author on reasonable request.

Author contribution

Ping Hu: Conceptualization, Methodology, Software, Writing - original draft; Writing - review & editing. **Ditho Pulungan**: Software, Methodology, Writing - review & editing. **Gilles Lubineau**: Supervision, Methodology, Conceptualization, Writing - review & editing.

CRediT authorship contribution statement

Gilles Lubineau: Conceptualization, Methodology, Supervision, Writing - original draft, Writing - review & editing, M.A: Conceptualization, Methodology, Supervision. A.Y: Conceptualization, Methodology, Supervision R.T. and X.L.: investigation, Data Curation.

Declaration of competing interest

The authors declare that they have no known competing financial interests or personal The authors declare that they have no known competing financial interests or personal relationships that could have appeared to influence the work reported in this paper.

Acknowledgement

The research reported in this publication was supported by funding from King Abdullah University of Science and Technology (KAUST) Baseline Research Funds, under award number BAS/1/1315-01-01.

References

[1] P. Johnson, F.K. Chang, Characterization of matrix crack-induced laminate failure—part i: Experiments, J. Compos. Mater. 35 (22) (2001) 2009–2035.
[2] B. Daum, N. Feld, O. Allix, R. Rolfes, A review of computational modelling approaches to compressive failure in laminates, Compos. Sci. Technol. 181 (2019) 107663.
[3] K.A. Kalteremidou, M. Hajikazemi, W.V. Paepegem, D.V. Hemelrijck, L. Pyl, Effect of multiaxiality, stacking sequence and number of off-axis layers on the mechanical

response and damage sequence of carbon/epoxy composite laminates under static loading, Compos. Sci. Technol. 190 (2020) 108044.
[4] C. Canturri, E.S. Greenhalgh, L.E. Asp, S.T. Pinho, Fractographic study to characterise the interaction between intralaminar and interlaminar fracture from embedded defects under compression loading, Compos. Appl. Sci. Manuf. 125 (2019) 105557.
[5] A. Quintanas-Corominas, A. Turon, J. Reinoso, E. Casoni, M. Paggi, J.A. Mayugo, A phase field approach enhanced with a cohesive zone model for modeling delamination induced by matrix cracking, Comput. Methods Appl. Mech. Eng. 358 (2020) 112618.
[6] A. Wagih, P. Maimí, N. Blanco, J. Costa, A quasi-static indentation test to elucidate the sequence of damage events in low velocity impacts on composite laminates, Compos. Appl. Sci. Manuf. 82 (2016) 180–189.
[7] M. Kashtalyan, C. Soutis, Analysis of composite laminates with intra- and interlaminar damage, Prog. Aero. Sci. 41 (2) (2005) 152–173.
[8] X.C. Sun, S.R. Hallett, Barely visible impact damage in scaled composite laminates: experiments and numerical simulations, Int. J. Impact Eng. 109 (2017) 178–195.
[9] M.R. Wisnom, S.R. Hallett, The role of delamination in strength, failure mechanism and hole size effect in open hole tensile tests on quasi-isotropic laminates, Compos. Appl. Sci. Manuf. 40 (4) (2009) 335–342.
[10] E. Abisset, F. Daghia, X.C. Sun, M.R. Wisnom, S.R. Hallett, Interaction of inter-and intralaminar damage in scaled quasi-static indentation tests: Part 1–experiments, Compos. Struct. 136 (2016) 712–726.
[11] X.C. Sun, M.R. Wisnom, S.R. Hallett, Interaction of inter- and intralaminar damage in scaled quasi-static indentation tests: Part 2 - numerical simulation, Compos. Struct. 136 (2016) 727–742.
[12] X. Lu, B.Y. Chen, V.B.C. Tan, T.E. Tay, A separable cohesive element for modelling coupled failure in laminated composite materials, Compos. Appl. Sci. Manuf. 107 (2018) 387–398.
[13] R. Higuchi, T. Okabe, T. Nagashima, Numerical simulation of progressive damage and failure in composite laminates using xfem/czm coupled approach, Compos. Appl. Sci. Manuf. 95 (2017) 197–207.
[14] G. Vigueras, F. Sket, C. Samaniego, L. Wu, L. Noels, D. Tjahjanto, E. Casoni, G. Houzeaux, A. Makradi, J.M. Molina-Aldareguia, M. Vázquez, A. Jérusalem, An xfem/czm implementation for massively parallel simulations of composites fracture, Compos. Struct. 125 (2015) 542–557.
[15] B.Y. Chen, S.T. Pinho, N.V. De Carvalho, P.M. Baiz, T.E. Tay, A floating node method for the modelling of discontinuities in composites, Eng. Fract. Mech. 127 (2014) 104–134.
[16] B.Y. Chen, T.E. Tay, S.T. Pinho, V.B.C. Tan, Modelling the tensile failure of composites with the floating node method, Comput. Methods Appl. Mech. Eng. 308 (2016) 414–442.
[17] J. Zhi, T.E. Tay, Explicit modeling of matrix cracking and delamination in laminated composites with discontinuous solid-shell elements, Comput. Methods Appl. Mech. Eng. 351 (2019) 60–84.
[18] M.Q. Le, H. Bainier, D. Néron, C. Ha-Minh, P. Ladevèze, On matrix cracking and splits modeling in laminated composites, Compos. Appl. Sci. Manuf. 115 (2018) 294–301.
[19] N. Moes, J. Dolbow, T. Belytschko, A finite element method for crack growth without remeshing 46 (09 1999) 131–150.
[20] T. Belytschko, R. Gracie, G. Ventura, A review of extended/generalized finite element methods for material modeling, Model. Simulat. Mater. Sci. Eng. 17 (4) (2009), 043001.
[21] P. Ladevèze, E. Le Dantec, Damage modelling of the elementary ply for laminated composites, Compos. Sci. Technol. 43 (3) (1992) 257–267.
[22] P. Ladevèze, G. Lubineau, D. Marsal, Towards a bridge between the micro- and mesomechanics of delamination for laminated composites, Compos. Sci. Technol. 66 (6) (2006) 698–712.
[23] G. Lubineau, P. Ladevèze, Construction of a micromechanics-based intralaminar mesomodel, and illustrations in ABAQUS/Standard, Comput. Mater. Sci. 43 (1) (2008) 137–145.
[24] E. Abisset, F. Daghia, P. Ladevèze, On the validation of a damage mesomodel for laminated composites by means of open-hole tensile tests on quasi-isotropic laminates, Compos. Appl. Sci. Manuf. 42 (10) (2011) 1515–1524.
[25] P. Hu, D. Pulungan, R. Tao, G. Lubineau, An experimental study on the influence of intralaminar damage on interlaminar delamination properties of laminated composites, Compos. Appl. Sci. Manuf. 131 (2020) 105783.
[26] M. Heidari-Rarani, M.M. Shokrieh, P.P. Camanho, Finite element modeling of mode I delamination growth in laminated DCB specimens with R-curve effects, Compos. B Eng. 45 (1) (2013) 897–903.
[27] Y. Gong, Y.X. Hou, L.B. Zhao, W.C. Li, J.Y. Zhang, N. Hu, A modified mode i cohesive zone model for the delamination growth in dcb laminates with the effect of fiber bridging, Int. J. Mech. Sci. 176 (2020), 105514.
[28] L.P. Canal, M. Alfano, J. Botsis, A multi-scale based cohesive zone model for the analysis of thickness scaling effect in fiber bridging, Compos. Sci. Technol. 139 (2017) 90–98.
[29] P.P. Camanho, C.G. Davila, M.F. De Moura, Numerical simulation of mixed-mode progressive delamination in composite materials, J. Compos. Mater. 37 (16) (2003) 1415–1438.
[30] ASTMD5528, Standard Test Method for Mode I Interlaminar Fracture Toughness of Unidirectional Fiber-Reinforced Polymer Matrix Composites, ASTM Internat, 2007.
[31] D. Pulungan, A. Yudhanto, G. Lubineau, Characterizing and modeling the progressive damage of off-axis thermoplastic plies: effect of ply confinement, Compos. Struct. 246 (2020) 112397.
[32] P. Ladevèze, G. Lubineau, On a damage mesomodel for laminates: micro–meso relationships, possibilities and limits, Compos. Sci. Technol. 61 (15) (2001) 2149–2158.
[33] P. Ladevèze, G. Lubineau, An enhanced mesomodel for laminates based on micromechanics, Compos. Sci. Technol. 62 (4) (2002) 533–541.
[34] Dassault Systemes Simulia Corp, Abaqus 6.12 Documentation, 2012.
[35] W.C. Cui, M.R. Wisnom, M. Jones, A comparison of failure criteria to predict delamination of unidirectional glass/epoxy specimens waisted through the thickness, Composites 23 (3) (1992) 158–166.
[36] M.L. Benzeggagh, M. Kenane, Measurement of mixed-mode delamination fracture toughness of unidirectional glass/epoxy composites with mixed-mode bending apparatus, Compos. Sci. Technol. 56 (4) (1996) 439–449.
[37] M.R. Abir, T.E. Tay, M. Ridha, H.P. Lee, On the relationship between failure mechanism and compression after impact (cai) strength in composites, Compos. Struct. 182 (2017) 242–250.
[38] F. Meier, C. Schwarz, E. Werner, Numerical calculation of the tangent stiffness matrix in materials modeling, Proc. Appl. Math. Mech. 14 (1) (12 2014) 425–426.
[39] Ran Tao, Xiaole Li, Arief Yudhanto, Marco Alfano, Gilles Lubineau, On controlling interfacial heterogeneity to trigger bridging in secondary bonded composite joints: an efficient strategy to introduce crack-arrest features, Compos. Sci. Technol. 188 (2020) 107964.
[40] Xiaole Li, Ran Tao, Marco Alfano, Gilles Lubineau, How variability in interfacial properties results in tougher bonded composite joints by triggering bridging, Int. J. Solid Struct. 191–192 (2020) 87–98.